*Supporting Information for:*

**Unconventional Molybdenum Carbide Phases with High Electrocatalytic Activity for Hydrogen Evolution Reaction**

Chaoyun Tang[abc], Hui Zhang[a], Kuofeng Xu[a], Qianling Zhang[a], Jianhong Liu[a], Chuanxin He[a], Liangdong Fan*[a] and Tewodros Asefa*[bcd]

[a]*College of Chemistry and Environmental Engineering, Shenzhen University, Shenzhen 518060, China. E-mail: fanld@szu.edu.cn*

[b]*Hoffmann Institute of Advanced Materials, Shenzhen Polytechnic, Shenzhen 518060, China.*

[c]*Department of Chemistry and Chemical Biology, Rutgers, The State University of New Jersey, 610 Taylor Road, Piscataway, New Jersey 08854, USA. E-mail: tasefa@chem.rutgers.edu*

[c]*Department of Chemical and Biochemical Engineering, Rutgers, The State University of New Jersey, 98 Brett Road, Piscataway, New Jersey 08854, USA.*
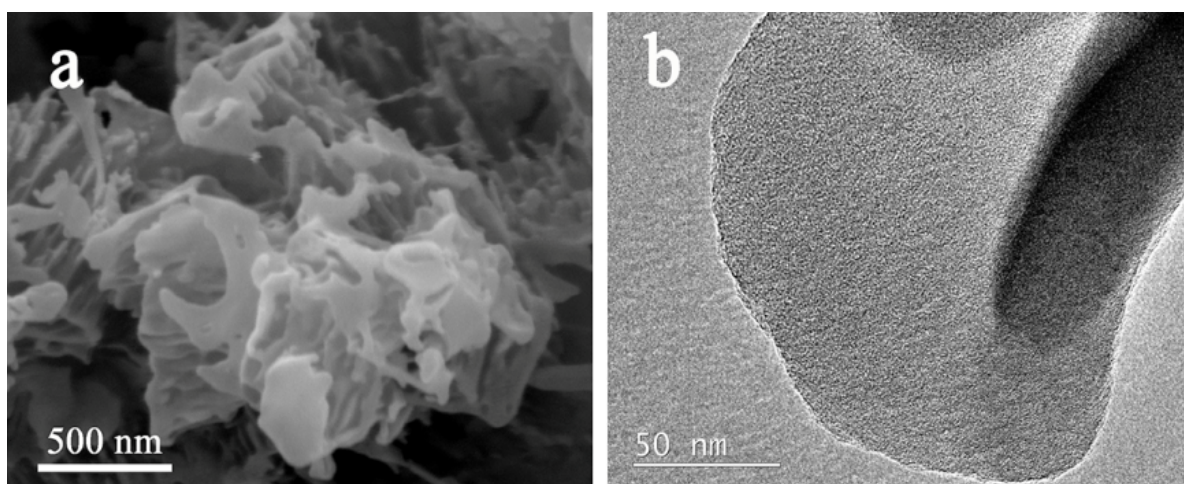
# 1. Additional Results



**Figure S1.** a) FESEM and b) TEM images of g-$C_3N_4$ prepared by directly pyrolyzing the CN hybrid material at 450 °C under a flow of $N_2$ gas.
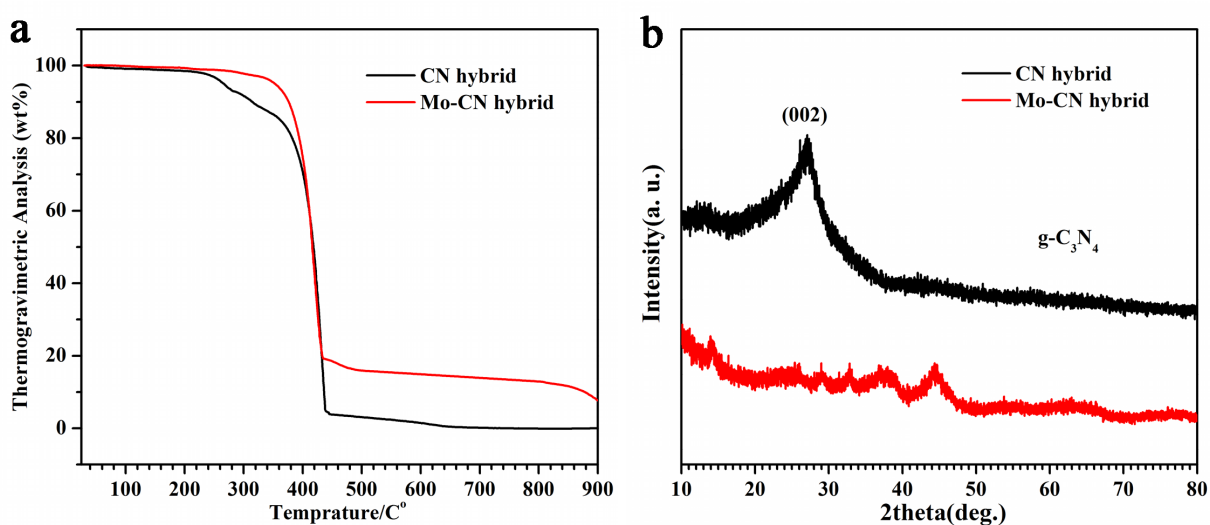


**Figure S2.** a) Thermogravimetric analysis (TGA) curves of CN hybrid material and Mo-CN hybrid material under $N_2$ atmosphere in the range of 30 to 900 °C at a heating rate of 10 °C/min. b) XRD patterns of the products obtained after pyrolysis of CN hybrid material and Mo-CN hybrid material at 450 °C in $N_2$ atmosphere. The results reveal that the thermal polycondensation of CN hybrid material forms g-$C_3N_4$, and the process ends before 450 °C. Furthermore, the result indicates that the presence of molybdate in CN hybrid material significantly affects the thermal polycondensation process, and also leads to a slightly different final product, as can be seen in the differences in the peaks observed in the red and black curves in b. The peaks in the red curve correspond predominantly to mixed oxides, $MoO_x$.
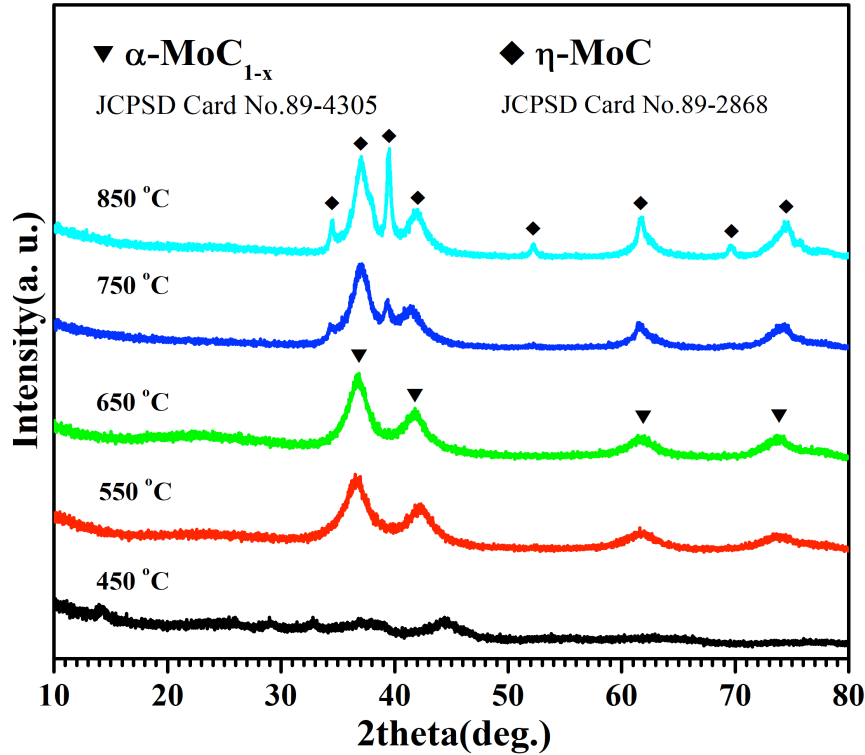
**Figure S3.** XRD patterns of Mo-CN hybrid material pyrolyzed at different temperatures. The products obtained after pyrolysis at 550 and 650 °C show Bragg peaks corresponding to $\alpha$-MoC$_{1-x}$ phase, and the products pyrolyzed at 750 and 850 °C show Bragg peaks corresponding to $\eta$-MoC phase. Due to their similarities, only the XRD patterns of products pyrolyzed at 650 and 750 °C are provided and and also discussed in more detail in the main text.
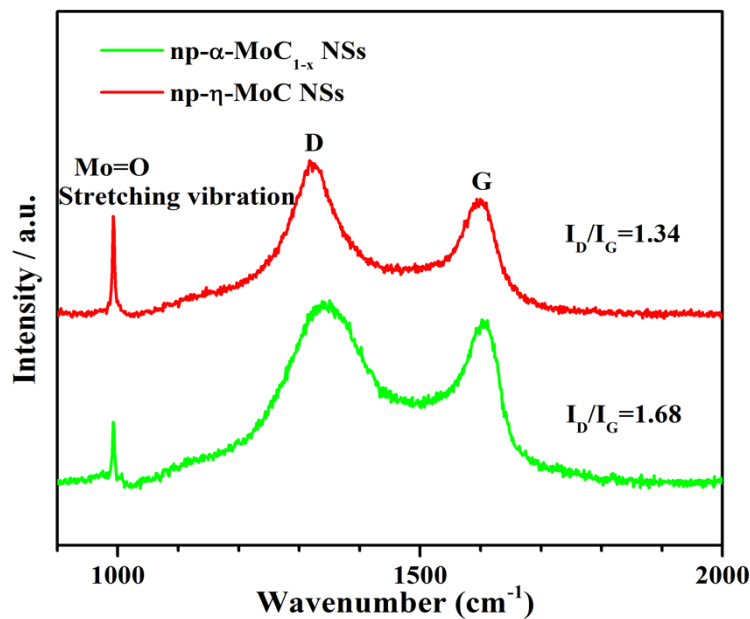


**Figure S4.** Raman spectra of as-prepared np-MoC NSs: $\alpha$-MoC$_{1-x}$ NSs and $\eta$-MoC NSs.
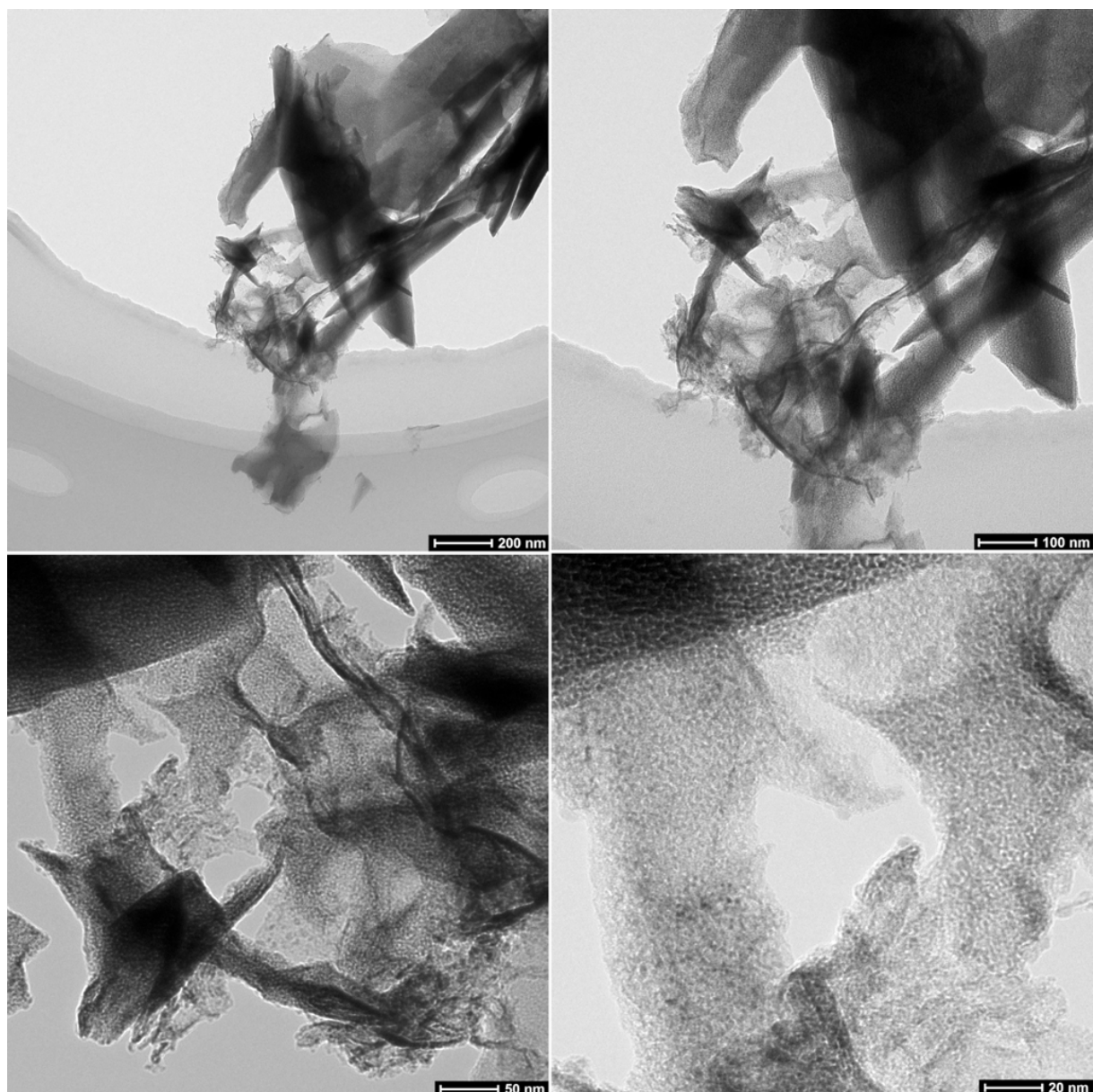
**Figure S5.** Typical TEM images of as-prepared np-$\alpha$-MoC$_{1-x}$ NSs in different resolutions.
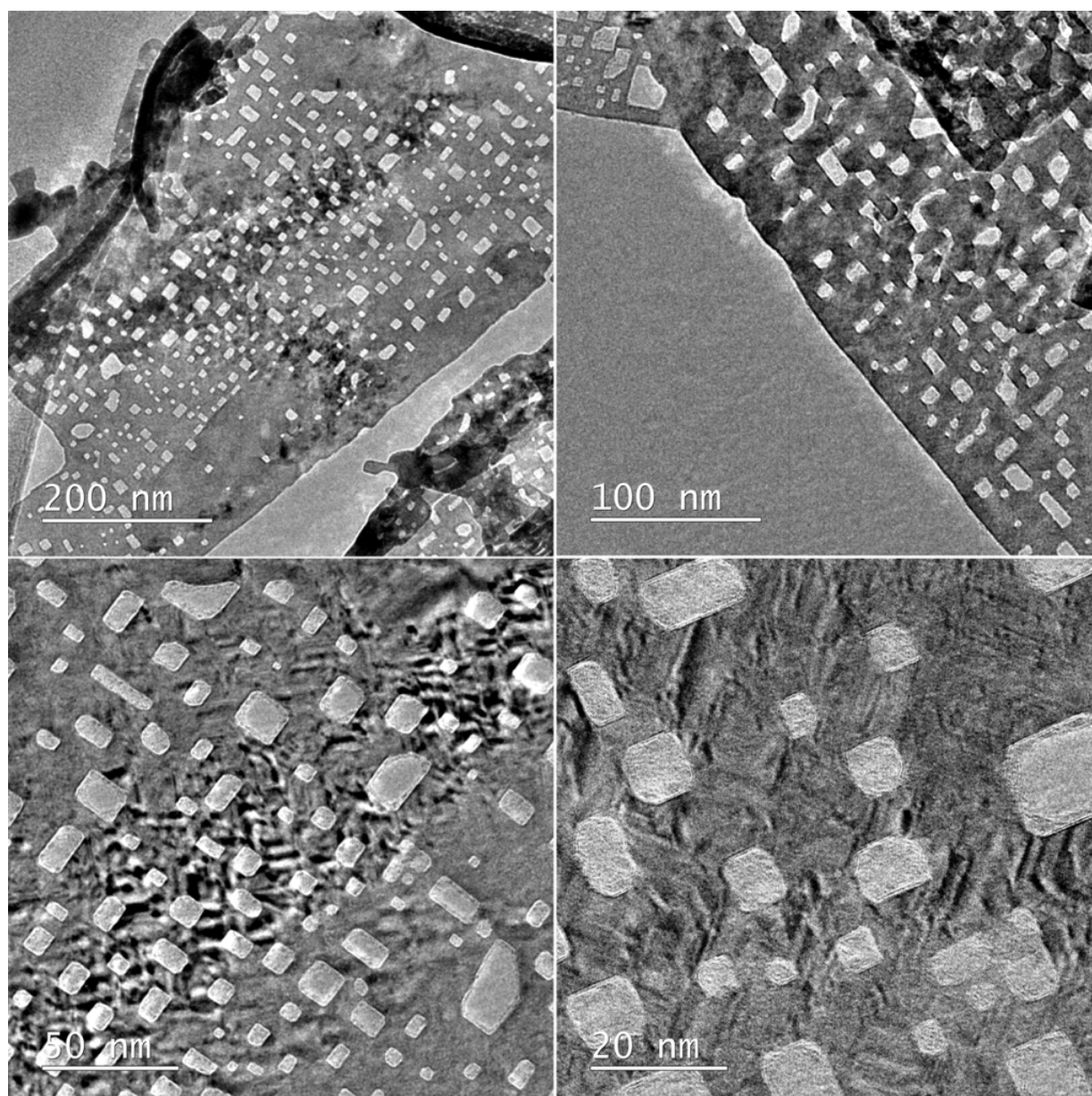
**Figure S6.** Typical TEM images of as-prepared np-$\eta$-MoC NSs in different resolutions.
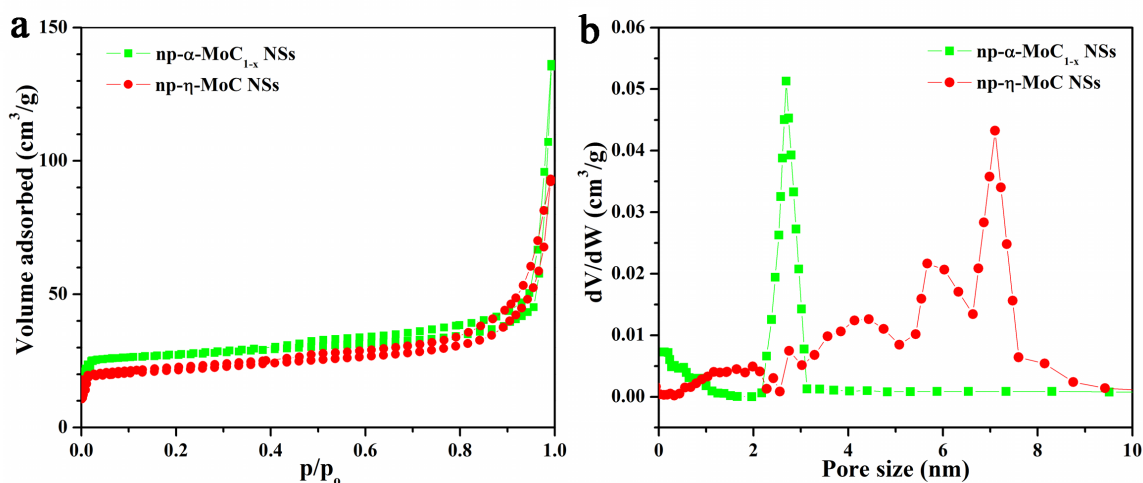
**Figure S7.** a) $N_2$ adsorption/desorption isotherms and b) pore size distributions of np-MoC NSs, namely $\alpha$-MoC$_{1-x}$ NSs and $\eta$-MoC NSs.

**Table S1.** Elemental compositions determined by a CHNOS analyzer of series materials obtained by pyrolysis of CN and Mo-CN hybrid materials at different temperatures.

| Elemental Composition | Materials | | | |
|---|---|---|---|---|
| | CN Hybrid Material Pyrolyzed at 450 °C | Mo-CN Hybrid Material Pyrolyzed at 450 °C | Mo-CN Hybrid Material Pyrolyzed at 650 °C (or np-$\alpha$-MoC$_{1-x}$ NSs) | Mo-CN Hybrid Material Pyrolyzed at 750 °C (or np-$\eta$-MoC NSs) |
| C (wt. %) | 35.62 | 8.32 | 14.16 | 11.62 |
| N (wt. %) | 62.31 | 13.21 | 0.26 | 0.23 |
| Mo (wt. %) | 0 | 54.83 | 85.03 | 87.72 |
| C/N Mole Ratio | 0.67 | 0.73 | 63.53 | 58.94 |
| C/Mo Mole Ratio | - | - | 1.33 | 1.06 |

The pyrolyzed CN hybrid material and Mo-CN hybrid material at 450 °C show similar molar ratio of C/N, which suggests that the formation of a $g$-C$_3$N$_4$ structure from Mo-CN hybrid just as in the one derived from CN hybrid material. Meanwhile, the O/Mo molar ratio for Mo-CN hybrid pyrolyzed at 450 °C is about 2.59, which suggest the existence of molybdenum oxide (MoO$_x$), where x can have values between 2 and 3. The Mo-CN hybrid material pyrolyzed at 650 °C and 750 °C show a C/Mo molar ratio of 1.33 and 1.06, respectively, which indicate the presence of insufficient carbon and the formation of substoichiometric molybdenum carbide.
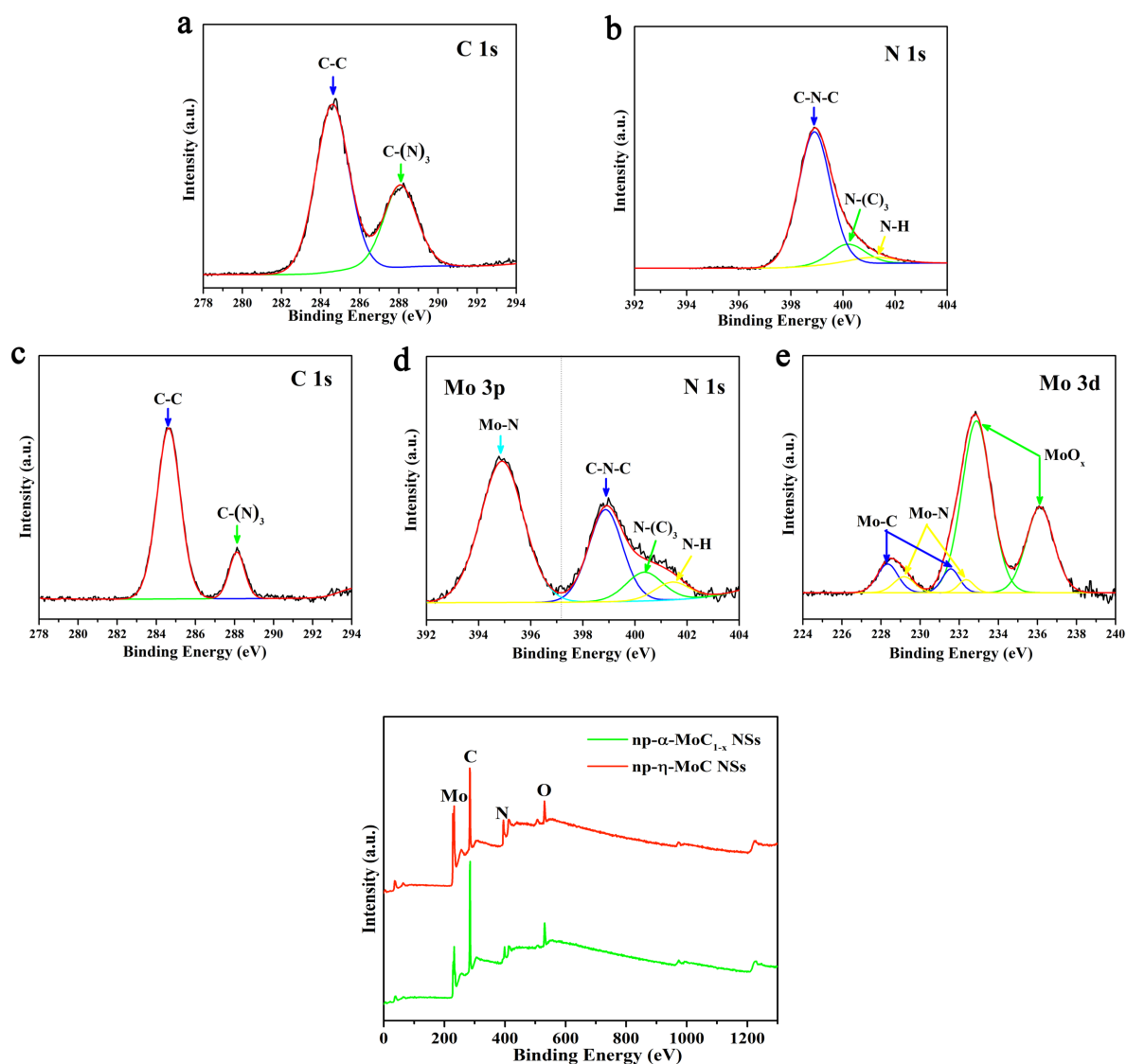
**Figure S8.** (a-e) High resolution, deconvoluted XPS spectra of different groups in samples produced from: (a and b) CN hybrid material by pyrolyis at 450 °C; and (c, d and e) Mo-CN hybrid material by pyrolysis at 450 °C. (f) Survey XPS spectra of Mo-CN hybrid material pyrolyzed at 650 °C (or np-$\alpha$-MoC$_{1-x}$ NSs) and at 750 °C (or np-$\eta$-MoC NSs).

The selection of the position of each peak for fitting is based on Giordano et al.[1] and calibrated on the basis of the position of C 1s peak. The two control samples prepared from CN hybrid material and Mo-CN hybrid material show similar C 1s spectra, the C-Mo peaks at 284.3 eV are much stronger than the C-N peaks at 286.3 eV, which is in line with the high C/N mol ratio. The CN hybrid material pyrolyzed at 450 °C shows typical XPS peaks of C 1s and N 1s. In N 1s spectrum, the Mo-N peaks at 395 eV and C-N peaks at 397.6 and 399.8 eV indicate the binding between N and Mo, C. The spectra also show an obvious Mo 3p peaks associated with Mo-N at 394.8 eV in N 1s spectrum. Meanwhile, the Mo 3d spectrum shows a doublet of Mo-C at 228.4 and 231.6 eV, and a doublet of Mo-N at 229.2 and 232.4 eV, suggesting a strong interaction between Mo and C as well as Mo and N. These results indicate the presence

of Mo-C and Mo-N bonding. The distinct peaks at 232.9 and 236.2 eV suggest the existence of MoO$_x$, which is most likely due to the surface oxidation of the materials during sample processing.[2]
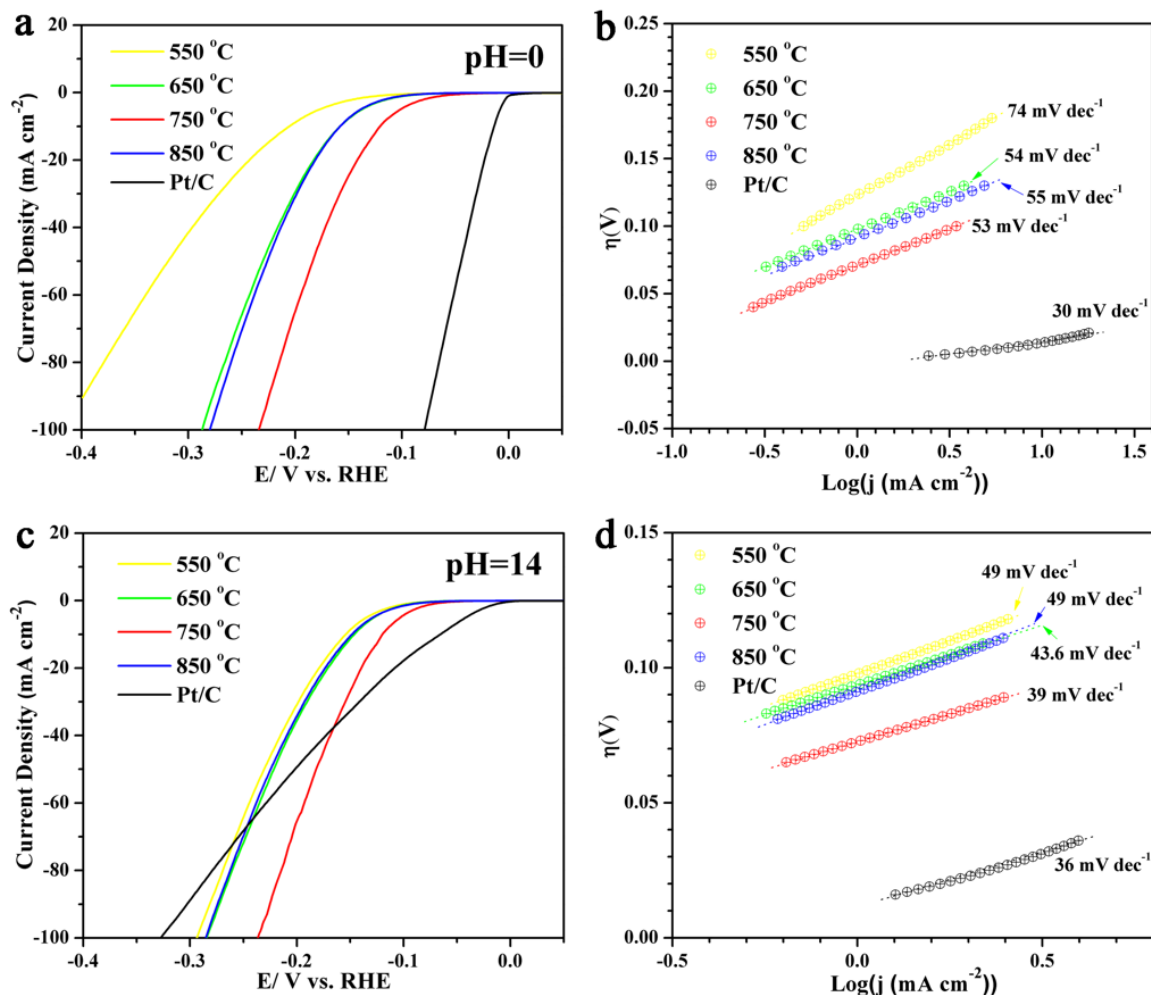


**Figure S9.** (a-d) Evaluation of the electrocatalytic properties toward HER in 0.5 M H$_2$SO$_4$ and 1 M KOH aqueous solutions of Mo-CN hybrid material pyrolyzed at different temperatures and Pt/C (a control catalyst): (a and c) polarization curves and (b and d) Tafel slopes. Due to the similarity in terms of phase and microstructure of the np-$\alpha$-MoC$_{1-x}$ NSs obtained by pyrolysis at 550 and 650 °C as well as the np-$\eta$-MoC NSs obtained by pyrolysis at 750 and 850 °C, only the results for the materials obtained by pyrolysis at 650 and 750 °C, or the two highly performing HER electrocatalysts, are displayed in the main text.
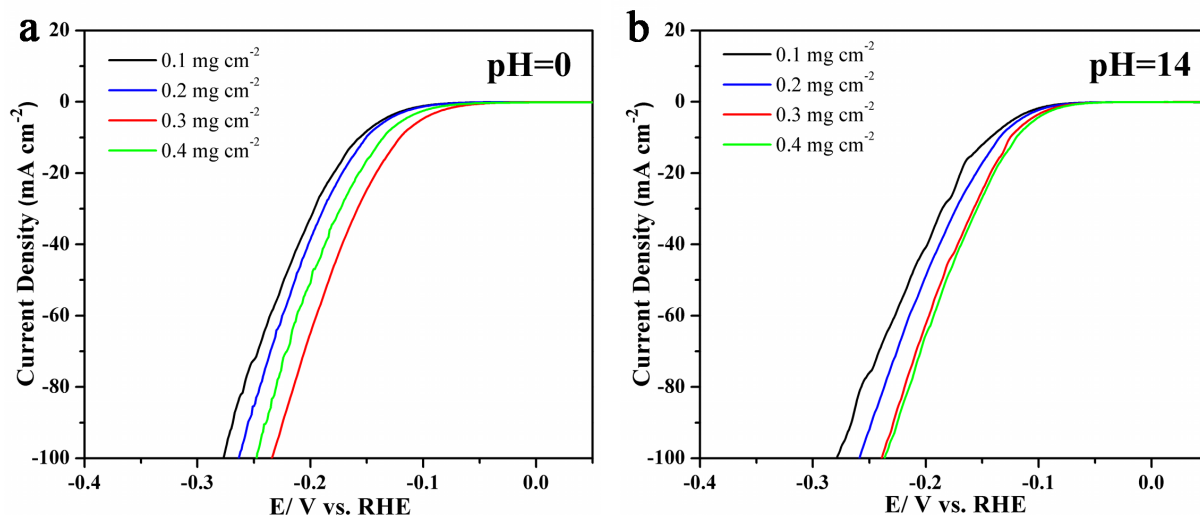
**Figure S10.** Polarization curves of HER over different amounts of as-synthesized np-$\eta$-MoC NSs catalysts on a glassy carbon (GC) electrode in a) 0.5 M $H_2SO_4$ and b) 1 M KOH solutions. It is obvious from the results that the optimal performance by the electrocatalysts for HER is exhibited when the loading of the catalyst is 0.3 mg cm$^{-2}$.
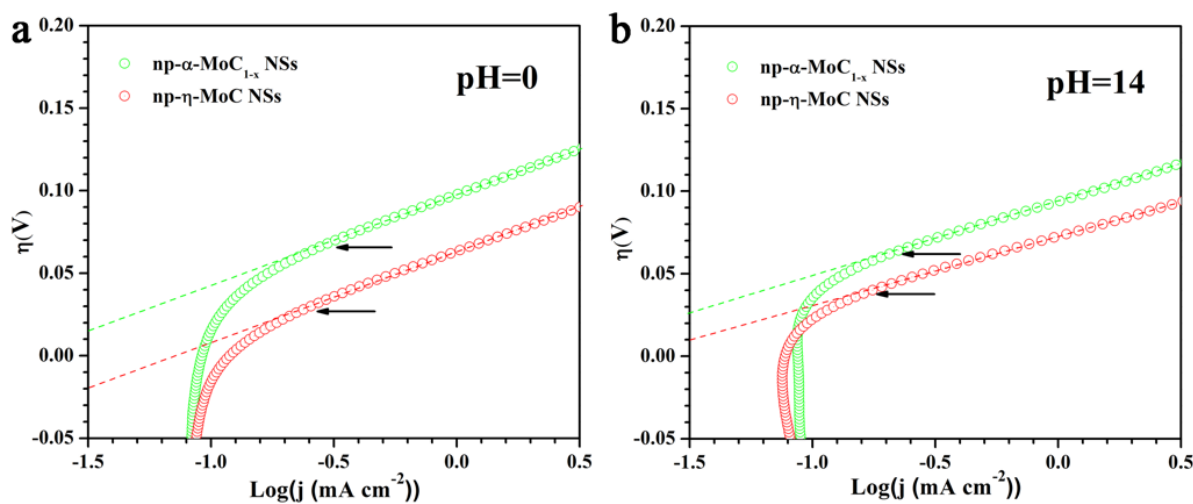


**Figure S11.** Tafel plots in the region of the low current density of two as-prepared np-$\alpha$-MoC$_{1-x}$ NSs and np-$\eta$-MoC NSs materials in a) 0.5 M $H_2SO_4$ and b) 1 M KOH solutions.
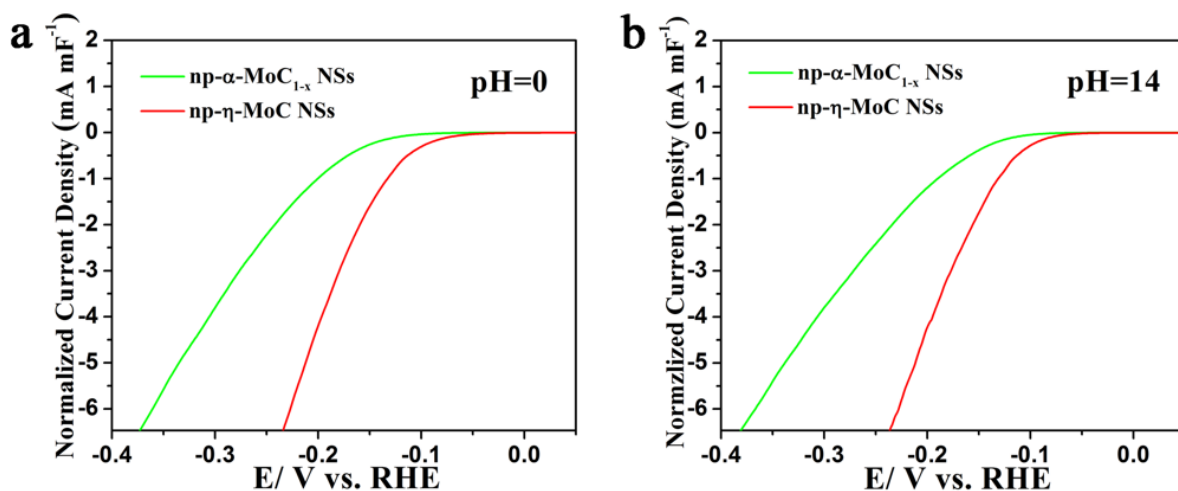
**Figure S12.** Nomolized current density by ESCA value of two as-prepared np-$\alpha$-MoC$_{1-x}$ NSs and np-$\eta$-MoC NSs materials during HER in a) 0.5 M H$_2$SO$_4$ and b) 1 M KOH solutions.



**Figure S13.** Capacitive current density from double layer charging versus potential of the two as-prepared np-MoC NSs: a) np-$\alpha$-MoC$_{1-x}$ NSs and b) np-$\eta$-MoC NSs. Continuous cyclic voltammetry sweeps are conducted in the region without Faradic current to obtain the results.

**Table S2.** Comparison of electrocatalytic activity toward HER in acidic media of different types of molybdenum carbides reported in the literature with those reported in this work.

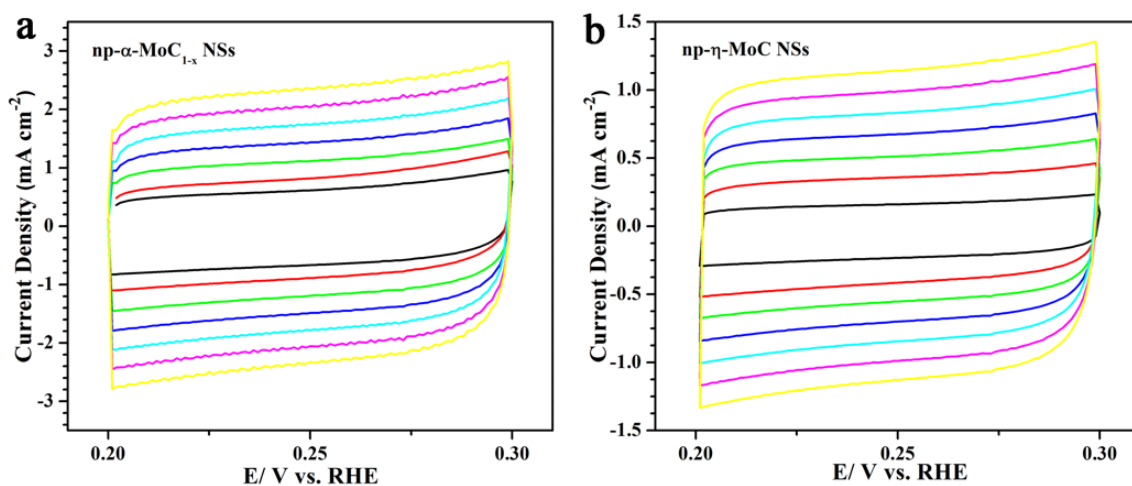| Catalyst | Electrolyte | Loading (mg/cm$^2$) | Tafel slope (mV/dec) | $\eta$ at 10 mA cm$^{-2}$ (mV) | Stability | References |
|---|---|---|---|---|---|---|
| $\beta$-Mo$_2$C | 1 M H$_2$SO$_4$ | 1.4 | 56 | 210 | 48 h | Angew. Chem. Int. Ed., 2012, **51**, 12703. |
| MoSoy ($\beta$-Mo$_2$C) | 0.1 M HClO$_4$ | 0.47 | 66.4 | 180 | 500 h | Energy Environ. Sci., 2013, **6**, 1818. |
| $\beta$-Mo$_2$C/CNT | 0.5 M H$_2$SO$_4$ | 2 | 55.2 | 150 | 3000 Cycles | Energy Environ. Sci., 2013, **6**, 943. |
| $\beta$-Mo$_2$C/RGO | 0.5 M H$_2$SO$_4$ | 0.285 | 57.3 | 130 | 1000 Cycles | Chem. Commun., 2014, **50**, 13135. |
| $\beta$-Mo$_2$C/CNT-GR | 0.5 M H$_2$SO$_4$ | 0.65 | 58 | 130 | 1000 Cycles | ACS Nano, 2014, **8**, 5164. |
| $\beta$-Mo$_2$C nanorods | 0.5 M H$_2$SO$_4$ | 0.43 | 58 | 150 | 2000 Cycles | Appl. Catal. B, 2014, **154−155**, 232. |
| np-$\beta$-Mo$_2$C NWs | 0.5 M H$_2$SO$_4$ | 0.21 | 53 | 135 | 25 h | Energy Environ. Sci., 2014, 7, 387. |
| $\alpha$-Mo$_2$C | 0.5 M H$_2$SO$_4$ | 0.102 | 58 | 198 | 1000 Cycles | J. Mater. Chem. A, 2015, **3**, 8361. |
| $\beta$-Mo$_2$C nanotubes | 0.5 M H$_2$SO$_4$ | 0.75 | 62 | 172 | 8 h | Angew. Chem. Int. Ed., 2015, **54**, 15395. |
| $\beta$-Mo$_2$C@NC | 0.5 M H$_2$SO$_4$ | 0.28 | 60 | 124 | 80 h | Angew. Chem., 2015, **127**, 10907. |
| $\beta$-MoCN-3D | 0.5 M H$_2$SO$_4$ | 0.26 | 51.4 | 89 | 10 h | NPG Asia Mater., 2016, **8**, e293. |
| Pomegranate-like β-Mo$_2$C@C | 0.5 M H$_2$SO$_4$ | 0.9 | 56 | 141 | 2000 Cycles | ACS Nano, 2016, **10**, 8851. |
| $\beta$-Mo$_2$C/NCF | 0.5 M H$_2$SO$_4$ | 0.28 | 55 | 144 | 8 h | ACS Nano, 2016, **10**, 11337. |
| $\eta$-MoC octahedrons | 0.5 M H$_2$SO$_4$ | 0.8 | 53 | 142 | 3000 Cycles | Nat. Commun., 2015, **6**, 6512. |
| $\eta$-MoC | 0.5 M H$_2$SO$_4$ | 0.14 | 62 | 232 | 3000 Cycles | Chem. Sci., 2016, **7**, 3399. |
| $\alpha$-MoC$_{1-x}$@BCN $\eta$-MoC@BCN | 0.5 M H$_2$SO$_4$ | 0.7-0.8 | 47 67 | 124 182 | 3000 Cycles | J. Mater. Chem. A, 2017, **5**, 13122. |
| $\alpha$-MoC$_{1-x}$ | 0.5 M H$_2$SO$_4$ | 0.3 | 54 | 158 | 5000 Cycles | **This work** |
| $\eta$-MoC | 0.5 M H$_2$SO$_4$ | 0.3 | 53 | 122 | 5000 Cycles | **This work** |

**Table S3.** Comparison of the electrocatalytic activities for HER in alkaline media of different molybdenum carbides reported in the literature with respect to those reported in this work.

| Catalyst | Electrolyte | Loading (mg/cm$^2$) | Tafel slope (mV/dec) | η at 10 mA cm$^2$ (mV) | Stability | References |
|---|---|---|---|---|---|---|
| $\beta$-Mo$_2$C | 1 M KOH | 1.4 | 54 | 190 | 48 h | Angew. Chem. Int. Ed., 2012, **51**, 12703. |
| $\beta$-Mo$_2$C nanorods | 1 M KOH | 0.43 | 45 | 130 | 2000 Cycles | Appl. Catal. B, 2014, **154−155**, 232. |
| $\alpha$-Mo$_2$C | 1 M KOH | 0.102 | 56 | 176 | 1000 Cycles | J. Mater. Chem. A, 2015, **3**, 8361. |
| $\beta$-Mo$_2$C nanotubes | 0.1 M KOH | 0.75 | 55 | 112 | 8 h | Angew. Chem. Int. Ed., 2015, **54**, 15395. |
| $\beta$-MoCN-3D | 1 M KOH | 0.26 | 78.4 | 122 | 10 h | NPG Asia Mater., 2016, **8**, e293. |
| Pomegranate-like $\beta$-Mo$_2$C@C | 1 M KOH | 0.9 | 71 | 47 | 2000 Cycles | ACS Nano, 2016, **10**, 8851. |
| $\beta$-Mo$_2$C/NCF | 1 M KOH | 0.28 | 65 | 100 | 8 h | ACS Nano, 2016, **10**, 11337. |
| $\eta$-MoC octahedrons | 1 M KOH | 0.8 | 59 | 151 | 3000 Cycles | Nat. Commun., 2015, **6**, 6512. |
| $\eta$-MoC | 1 M KOH | 0.14 | 56 | 225 | 3000 Cycles | Chem. Sci., 2016, **7**, 3399. |
| $\alpha$-MoC$_{1-x}$@BCN $\eta$-MoC@BCN | 1 M KOH | 0.7-0.8 | 98 55.4 | 154 106 | 3000 Cycles | J. Mater. Chem. A, 2017, **5**, 13122. |
| $\alpha$-MoC$_{1-x}$ | 1 M KOH | 0.3 | 43.6 | 147 | 5000 Cycles | **This work** |
| $\eta$-MoC | 1 M KOH | 0.3 | 39 | 119 | 5000 Cycles | **This work** |

## 2. Theoretical calculations

Density functional theory (DFT) calculations were performed with the Vienna *ab initio* simulation package (VASP).[3,4] The generalized gradient approximation (GGA) expressed *via* the Perdew-Burke-Ernzerhof (PBE) exchange correlation functional[5] and a plane-wave cutoff energy of 350 eV were used for all the computations. The ion-electron interaction was described by the projector-augmented plane wave (PAW) pseudopotentials.[6,7] The correlative theoretical models were constructed to simulate the $\alpha$-MoC$_{1-x}$ and $\eta$-MoC phases as well as the N-doped phases, which are denoted as $\alpha$-MoC$_{1-x}$@N and $\eta$-MoC@N, respectively (Figure S13). The lattice constants along x, y and z directions are 8.77, 8.77 and 20.00 Å for $\alpha$-MoC$_{1-x}$ and $\alpha$-MoC$_{1-x}$@N; and 14.99, 6.03 and 20.00 Å for $\eta$-MoC and $\eta$-MoC@N (Table S4). Specifically, the (001) facet of $\alpha$-MoC$_{1-x}$, which has been predicted to be the most stable surface on these materials,[8] was adopted to act as the catalytic active surface. The (104) facet of $\eta$-MoC was adopted to act as the catalytic active surface due to the preferable orientation of this facet in the materials, as observed in TEM images. All the structures were fully relaxed until all forces were less than 0.02 eV/Å, and the convergence threshold in energy was set as $10^{-5}$ eV. For geometric optimization of $\alpha$-MoC$_{1-x}$ and $\eta$-MoC, 4×4×1 and 2×4×1 Monkhorst-Pack grid *k*-point meshes, respectively, were used.

The free energies of adsorbed H ($\Delta G_{H*}$) on different surfaces were calculated using the equation:

$$\Delta G_{H*} = \Delta E_{H*} + \Delta ZPE - T\Delta S$$

where $\Delta E_{H*}$ is the binding energy, $\Delta ZPE$ is the change in zero-point energy, $T$ is the system temperature (which is 300 K, in our work) and $\Delta S$ is the change in entropy of H* adsorption.

In this work, the $\Delta E_{H*}$ was calculated using the equation:

$$\Delta E_{H*} = E_{final} - E_{substrate} - E_{adsorbate}$$

where $E_{final}$, $E_{substrate}$ and $E_{adsorbate}$ represent the total energy of adsorbate on substrate, the total energy of substrate and the total energy of adsorbate, respectively. Higher negative

values of $\Delta E_{H*}$ indicate stronger adsorption. The $\Delta ZPE$ and $T\Delta S$ are obtained based on the scheme proposed by Nørskov *et al.*[9] Specifically, $\Delta ZPE$ can be calculated using the equation $\Delta ZPE = ZPE(H^*) - 1/2\ ZPE(H_2)$. The value of calculated $ZPE(H_2)$ is *ca.* 0.282 eV. $\Delta S$ can be calculated by using the equation $\Delta S = S(H^*) - 1/2\ S(H_2) \approx -1/2\ S(H_2)$ and by considering the vibrational entropy of H* to be negligible. The corresponding $T\Delta S$ value is considered to be -0.205 eV, because $TS(H_2)$ is known to be 0.41 eV for $H_2$ at 300 K and 1 atm.[10] In Table S4, all the computed $ZPE(H^*)$ for H* adsorbed on the surfaces of different model structures and the corresponding $\Delta ZPE - T\Delta S$ as well as $\Delta E(H^*)$ values are compiled.

Finally, the free energy of adsorbed H ($\Delta G_{H*}$) on pure $\alpha$-MoC$_{1-x}$ phase, pure $\eta$-MoC phase and N-doped phases are obtained. The value of $\Delta G_{H*}$ is widely considered as an effective descriptor of the intrinsic electrocatalytic activity material for HER.[11] Promising hydrogen-evolving materials have $\Delta G_{H*}$ values of approximately zero. $\beta$-Mo$_2$C phase has been reported to have a $\Delta G_{H*}$ value of about -0.84 eV.[10,12] For pure MoC materials, the adsorption site of H is generally located at the three-fold sites on the Mo-terminated surface.[13] The computed $\Delta G_{H*}$ values of pure $\alpha$-MoC$_{1-x}$ and $\eta$-MoC phases are found to be -1.565 and -1.035 eV, respectively, which are relative higher than that of $\beta$-Mo$_2$C phase. The means the former two can be expected to display an inferior electrocatalytic activity for HER. However, when the N atom substitutes a C atom as the adsorption site of H, the computed $\Delta G_{H*}$ values of the resulting materials, $\alpha$-MoC$_{1-x}$@N and $\eta$-MoC@N, decrease and become closer to zero, indicating a considerably higher electrocatalytic activity of these materials for HER. The results demonstrate the N atom doping can serve as an effective way to promote the intrinsic HER activity of MoC materials.

**Table S4.** The lattice parameters (Å) of the supercells for all the model systems studied above.

| Models | a | b | c |
|---|---|---|---|
| $\alpha$-MoC$_{1-x}$<br>$\alpha$-MoC$_{1-x}$@N | 8.77 | 8.77 | 20.00 |

| | | | |
|---|---|---|---|
| $\eta$-MoC $\eta$-MoC@N | 14.99 | 6.03 | 20.00 |

**Table S5.** The adsorption energy of H species ($\Delta E_{H*}$), the relevant contributions to the free energy ($\Delta ZPE - T\Delta S$), and the free energy of adsorbed H ($\Delta G_{H*}$) on different surfaces.

| Models | $\Delta E_{H*}$ (eV) | ZPE(H*)/eV | $\Delta$ZPE-T$\Delta$S (eV) | $\Delta G_{H*}$ (eV) |
|---|---|---|---|---|
| $\alpha$-MoC$_{1-x}$ | -1.23 | 0.011 | -0.335 | -1.565 |
| $\alpha$-MoC$_{1-x}$@N | -0.04 | 0.071 | -0.275 | -0.315 |
| $\eta$-MoC | -0.72 | 0.031 | -0.315 | -1.035 |
| $\eta$-MoC@N | 0.09 | 0.061 | -0.285 | -0.195 |

α-MoC$_{1-x}$

α-MoC$_{1-x}$@N

η-MoC

η-MoC@N

Front view

Mo atom

C atom

N atom

H atom
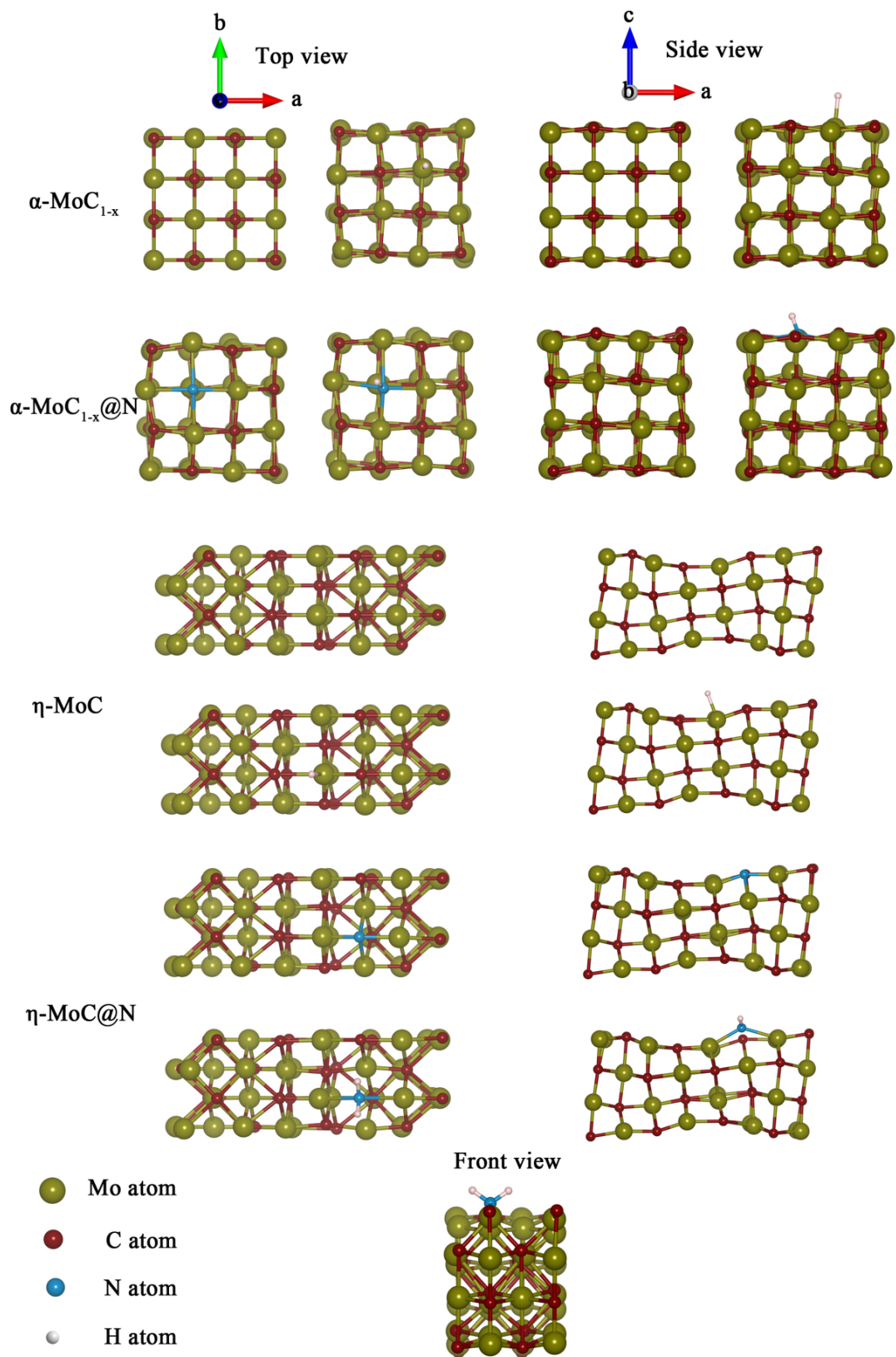
**Figure S14.** The theoretical models used for DFT calculations: $\alpha$-MoC$_{1-x}$, $\alpha$-MoC$_{1-x}$@N, $\eta$-MoC and $\eta$-MoC@N. They were used to calculate the Gibbs free energy of adsorbed H* on their surfaces.

## References

(1) C. Giordano, C. Erpen, W. Yao and M. Antonietti, *Nano Lett.* 2008, **8**, 4659-4663.

(2) C. Tang, W. Wang, A. Sun, C. Qi, D. Zhang, Z. Wu and D. Wang, *ACS Catal.* 2015, **5**, 6956-6963.

(3) G. Kresse and J. Hafner, *Phys. Rev. B* 1993, **47**, 558.

(4) G. Kresse and J. Hafner, *Phys. Rev. B* 1994, 49, 14251.

(5) J. P. Perdew, K. Burke and M. Ernzerhof, *Phys. Rev. Lett.* 1996, **77**, 3865.

(6) P. E. Blochl, *Phys. Rev. B* 1994, **50**, 17953.

(7) G. Kresse and D. Joubert, *Phys. Rev. B* 1999, **59**, 1758.

(8) J. R. dos Santos Politi, F. Vines, J. A. Rodriguez and F. Illas, *Phys. Chem. Chem. Phys.* 2013, **15**, 12617.

(9) J. K. Nørskov, T. Bligaard, A. Logadottir, J. R. Kitchin, J. Chen, S. Pandelov and U. Stimming, *J. Electrochem. Soc.* 2005, **152**, J23.

(10) Y. Liu, G. Yu, G. Li, Y. Sun, T. Asefa, W. Chen and X. Zou, *Angew. Chem.* 2015, **127**, 10902.

(11) J. K. Nørskov, T. Bligaard, A. Logadottir, J. R. Kitchin, J. Chen, S. Pandelov and U. Stimming, *J. Electrochem. Soc.* 2005, **152**, J23.

(12) J. Li, Y. Wang, C. Liu, S. Li, Y. Wang, L. Dong, Z. Dai, Y. Li and Y. Lan, *Nat. Commun.* 2016, **7**, 11204.

(13) J. Ren, C. Huo, J. Wang, Z. Cao, Y. Li and H. Jiao, *Surf. Sci.* 2006, **600**, 2329.